



## Energy materials

# Application of murexide as a capping agent for fabrication of magnetite anodes for supercapacitors: experimental and first-principle studies

Coulton Boucher<sup>1</sup>, Dalve Tang<sup>1</sup>, Igor Zhitomirsky<sup>1</sup>, and Oleg Rubel<sup>1,\*</sup>

<sup>1</sup> Department of Materials Science and Engineering, McMaster University, 1280 Main Street West, Hamilton, ON L8S 1G1, Canada

**Received:** 17 November 2023

**Accepted:** 16 February 2024

**Published online:**

19 March 2024

© The Author(s), under exclusive licence to Springer Science+Business Media, LLC, part of Springer Nature, 2024

## ABSTRACT

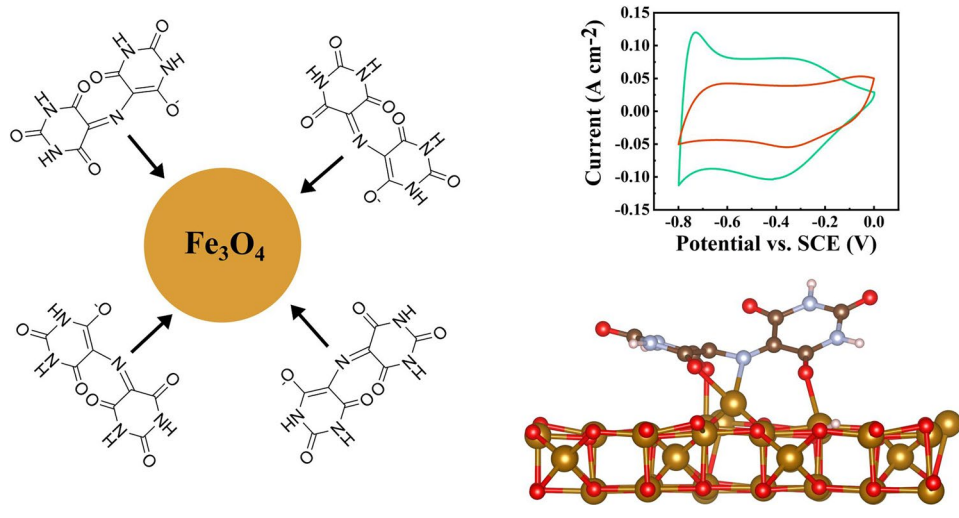
In this study, we investigate the effectiveness of murexide for surface modification of  $\text{Fe}_3\text{O}_4$  nanoparticles to enhance the performance of multiwalled carbon nanotube- $\text{Fe}_3\text{O}_4$  supercapacitor anodes. Our experimental results demonstrate significant improvements in electrode performance when murexide is used as a capping or dispersing agent compared to the case with no additives. When murexide is used as a capping agent, we report a capacitance of  $4.2 \text{ F cm}^{-2}$  from cyclic voltammetry analysis with good capacitance retention at high scan rates. From impedance measurements, we reveal a substantial decrease in the real part of impedance for samples prepared with murexide, indicating easier charge transfer at more negative electrode potentials, and reinforcing the role of murexide as a capping agent and charge transfer mediator. Density functional theory is used to investigate interactions between the murexide adsorbate and the  $\text{Fe}_3\text{O}_4$  (001) surface, with a specific emphasis on adsorption strength, charge transfer, and electronic properties. This theoretical investigation uncovers a strong adsorption enthalpy of  $-4.5 \text{ eV}$  and allows us to identify the nature of chemical bonds between murexide and the surface, with significant charge transfer taking place between the  $\text{Fe}_3\text{O}_4$  surface and murexide adsorbate. The transfer of electrons from the  $\text{Fe}_3\text{O}_4$  surface to murexide is recognized as a vital component of the adsorption process. By examining the bonding nature of murexide on  $\text{Fe}_3\text{O}_4$ , this research study uncovers insights and proposes a novel bonding configuration of murexide that incorporates a combination of bridging and chelating bonding.

Handling Editor: Kevin Jones.

Address correspondence to E-mail: rubelo@mcmaster.ca

E-mail Addresses: bouchc1@mcmaster.ca; tangd8@mcmaster.ca; zhitom@mcmaster.ca

## GRAPHICAL ABSTRACT



## Introduction

Supercapacitors have emerged as promising energy storage devices due to their high power density, fast charging and discharging rates, and long cycle life [1]. Advanced electrode materials play a critical role in the electrochemical performance of supercapacitors, as they are responsible for storing and releasing charge during the charge/discharge cycles [2]. However, the electrochemical performance of these materials can be limited by factors such as low surface area, poor wettability, and high resistance at the electrode–electrolyte interface.

Surface modification has been identified as a key strategy to overcome these limitations and enhance the electrochemical performance of anode materials for supercapacitor applications [3, 4]. Surface modification techniques such as surface roughening, the use of nanostructured materials, and the control of surface chemistry can increase the surface area, improve the wettability, and reduce the resistance at the electrode–electrolyte interface [5–7]. These modifications can lead to higher capacitance and energy density, improved rate capability, and cycling stability of supercapacitors.

By utilizing distinct materials for the anode and cathode, a supercapacitor device can optimize its operational voltage window by capitalizing on the unique potential ranges offered by each electrode [8]. Such an asymmetric device, containing  $\text{Fe}_3\text{O}_4$  and  $\text{MnO}_2$  electrodes, can exhibit an expanded voltage window of

1.8 V in aqueous  $\text{K}_2\text{SO}_4$  electrolyte and have a reported capacitance of  $50 \text{ F g}^{-1}$  at electrode mass density of  $8.8 \text{ mg cm}^{-2}$  [9]. However, the negative electrodes display a significantly lower gravimetric capacitance than the positive electrodes, leading to a greater active mass in the negative electrode needed to match the capacitance of the positive electrode. This emphasizes the need to increase the specific capacitance of the negative electrodes, while ensuring excellent performance at high active mass. Designing electrodes with high active mass poses several challenges, including the poor charge transfer between  $\text{Fe}_3\text{O}_4$  and conductive additives. Metal oxide nanoparticles and carbon nanotubes (CNTs) have high surface areas, making them prone to agglomeration, which further complicates the charge transfer process. Additionally, a decline in specific capacitance is observed as the active mass of capacitive material increases, primarily due to the weak electronic and ionic conductivities [10] of metal oxide-based electrodes.

Recently, significant interest has been generated in application of chelating molecules for surface modification of materials [11]. The strong adsorption of such molecules on particle surface is an important factor for many applications. Molecules of different types are currently under investigation, including catecholates, gallates, salicylates, and other molecules from phosphonic acid and chromotropic acid families [3, 11]. Such molecules show strong bidentate or tridentate bonding to metal atoms on the particle surface, which is critical for their applications as capping agents for

synthesis of nanoparticles, dispersing agents for colloidal processing and extractors for liquid–liquid extraction of nanoparticles [3, 11, 12]. Surface modification of metal oxide nanoparticles was used for their improved dispersion in different solvents [13–16]. Of particular interest are applications of catecholates as photosensitizers for surface modification of semiconductors for photovoltaic applications [17]. Catecholates were used as capping agents for synthesis of nanoparticles for supercapacitor electrodes with enhanced capacitive properties [6]. To enhance the capacitance of supercapacitor electrodes, a catecholate-type celestine blue molecule was employed as a capping agent during synthesis, a cationic dispersing agent for colloidal processing, and a charge transfer mediator [18].

Charge transfer mediators introduce a fast and reversible redox reaction that enhances the ionic conductivity and increases the pseudocapacitive capacity of the supercapacitor [19]. They can also store charges through valence changes and electron transfer between the mediators and electronic conductors, such as activated carbon, which provides additional charge capacity beyond that of electrostatic double-layer capacitors [20, 21]. Unlike pseudocapacitance, the redox mediator-induced capacitance is not dependent on the number of electrochemically active sites. The energy density of a redox mediator-based supercapacitor relies on the solubility of the redox mediators and their interaction with the electrodes. If highly soluble redox mediators are used, the volumetric energy density can be significantly improved as the dissolved mediator molecules or ions do not cause any significant volume changes in the entire system [22]. Roldán et al. [23] have shown that using hydroquinone as a redox mediator in an electrolyte supporting 1 M H<sub>2</sub>SO<sub>4</sub> with a chemically activated carbon electrode can result in a twofold increase in specific capacitance. This increase is due to the additional pseudocapacitive contribution from the faradaic reactions of the hydroquinone/quinone system in the redox electrolyte. These studies have generated interest in the search for charged chelating molecules with redox properties for the development of advanced supercapacitor electrodes.

Murexide is a versatile and widely used indicator in analytical chemistry. Murexide has been employed in complexometric investigations involving 3d or 4f ions, where the formation of a complex results in a modification of the solution's color [24–27]. It can form stable, colored complexes with a range of metal

ions, including transition metals such as iron, cobalt, nickel, and copper [28]. These complexes have distinctive hues that can be easily observed and quantified, making murexide an excellent tool for identifying and measuring metal ions in a sample. Furthermore, murexide can be employed in both aqueous and non-aqueous solvents, expanding its potential applications in a variety of fields [29].

Murexide has emerged as a promising capping and dispersing agent for the surface modification of cathode materials in supercapacitor applications [12, 30]. Murexide has been used as a capping agent for Mn<sub>3</sub>O<sub>4</sub> nanoparticles and as a co-dispersant for Mn<sub>3</sub>O<sub>4</sub> and CNTs. The adsorption of murexide on Mn<sub>3</sub>O<sub>4</sub> and CNTs facilitated electrostatic co-dispersion of Mn<sub>3</sub>O<sub>4</sub> with CNTs with enhanced mixing to significantly increase the performance of the Mn<sub>3</sub>O<sub>4</sub>-CNT electrodes [12].

The redox properties of murexide have been investigated in various solvents and electrolytes, and the results have shown that it can exhibit multiple redox peaks with low redox potentials and good reversibility in aqueous electrolytes, indicating its potential for high energy density applications. In aqueous electrolytes, reversible cathodic and anodic peaks are well defined in a voltage window of 0 to –1.5 V versus saturated calomel electrode (SCE) [29].

In this work, we are conducting the first density functional theory (DFT) study to investigate the adsorption mechanism and binding energy of murexide on a surface of Fe<sub>3</sub>O<sub>4</sub>. The bonding mechanism of murexide on surfaces remains poorly understood, and therefore, we propose a novel bonding configuration that utilizes four atoms in the murexide molecule, forming a combination of bridging and chelating bonds. This proposed configuration contrasts with the tridentate [12, 28, 31] bonding previously suggested in the literature and offers a promising explanation for the strong adsorption observed experimentally. The charge density and Bader charge analyses are performed to understand the mechanism of molecular adsorption and magnitude of charge transfer during the adsorption process. The results of this study provide insights into the underlying principles governing the interaction between murexide and Fe<sub>3</sub>O<sub>4</sub> and will help to identify the optimal conditions for using murexide as an effective adsorbent in various applications. To corroborate the theoretical findings with experimental results, we have fabricated Fe<sub>3</sub>O<sub>4</sub>-CNT composite electrodes using murexide as a capping and

dispersing agent. This study aims to investigate, for the first time, the difference in electrode performance when the same molecule is used strictly as a dispersing agent, or as a capping agent. This combination of theoretical and experimental approaches provides a comprehensive understanding of the behavior of murexide as a dispersant agent, capping agent, and charge transfer mediator, and its potential use in energy storage applications.

## Materials and methods

### Materials and experimental methods

Iron (II) chloride tetrahydrate, iron (III) chloride hexahydrate, ammonium hydroxide, murexide (ammonium 2,6-dioxo-5-[(2,4,6-trioxo-5-hexahydropyrimidinylidene)amino]-3H-pyrimidin-4-olate), poly(vinyl butyral-co-vinyl alcohol-co-vinyl acetate) (PVB, MilliporeSigma, Canada), multiwalled carbon nanotubes (MWCNT, ID 4 nm, OD 13 nm, length 1–2  $\mu\text{m}$ , Bayer, Germany), and nickel foam (porosity 95%, thickness 1.6 mm, Vale, Canada) were used as starting materials.

Synthesis of  $\text{Fe}_3\text{O}_4$  was performed by a chemical precipitation method [18, 32] using aqueous solutions of iron (II) chloride and iron (III) chloride. The molar ratio of  $\text{FeCl}_2$  to  $\text{FeCl}_3$  in the solutions was 1:2. For the synthesis of  $\text{Fe}_3\text{O}_4$  in the presence of MWCNT, a 3 g  $\text{L}^{-1}$  MWCNT suspension was initially prepared. Preparation included ultrasonication of the MWCNT suspensions using a high energy Cole-Parmer (Canada) ultrasonic processor. Iron (II) chloride tetrahydrate and iron (III) chloride hexahydrate were added to the suspension, allowing for an  $\text{Fe}_3\text{O}_4$ :MWCNT mass ratio of 4:1. The pH of the solutions was adjusted to pH=9 by ammonium hydroxide. Chemical precipitation was performed at 50 °C at continuous stirring. Obtained suspensions were separated via centrifuge, washed, filtrated, and dried overnight in an oven at 60 °C. For DE and DW samples,  $\text{Fe}_3\text{O}_4$ -MWCNT suspension was redispersed in ethanol and water, respectively, via ultrasonication before being separated, washed, filtrated, and dried. For C5 and C10 samples, murexide was added to the Fe salt solution during synthesis in a weight percentage of 5% and 10%, respectively, then separated, washed, filtrated, and dried.

Electrodes were prepared by impregnation of Ni foam current collectors with slurries, containing

$\text{Fe}_3\text{O}_4$ , MWCNT, and PVB binder. The mass ratio of  $\text{Fe}_3\text{O}_4$ :MWCNT:PVB was 80:20:3. The mass of the impregnated material after drying was 40 mg  $\text{cm}^{-2}$ . The impregnated Ni foams were pressed to 30% of their original thickness in order to improve electrical contact of the impregnated material and current collector.

Electrochemical studies were performed in aqueous 0.5 M  $\text{Na}_2\text{SO}_4$  electrolyte using Biologic VMP 300 potentiostat (BioLogic, France) for cyclic voltammetry (CV), electrochemical impedance spectroscopy (EIS), and galvanostatic charge–discharge (GCD) investigations. Testing was performed using a 3-electrode electrochemical cell containing a working electrode (impregnated Ni foam), counter-electrode (Pt mesh), and a reference electrode (SCE, saturated calomel electrode). Mass- and area-normalized capacitances were calculated from the corresponding CV and GCD data, as described by previous studies [33, 34]. The capacitances calculated from the CV and GCD data represented integral capacitances measured in a potential window of –0.8 ... 0 V versus SCE. The capacitances calculated from the EIS data represented differential capacitances measured at a potential 0 V, –0.2 V, –0.4 V, –0.6 V, and –0.8 V versus SCE, at voltage amplitude of 5 mV. CV results were obtained at 2, 5, 10, 20, 50, and 100 mV  $\text{s}^{-1}$  scan rates with EIS measurements performed afterward. GCD results were obtained at 3, 5, 7, 10, 20, 30, and 40 mA  $\text{cm}^{-2}$  current densities.

### Computational

The first-principles electronic structure calculations were performed in the framework of DFT [35] using Perdew–Burke–Ernzerhof (PBE) generalized gradient approximation [36] for the exchange–correlation functional, augmented by the DFT-D3 correction with Becke–Johnson damping [37, 38] to capture van der Waals interactions. The Vienna ab initio simulation program (VASP) (version 5.4.4, University of Vienna, Vienna, Austria) [39–41] and projector augmented-wave potentials [42] were used, where the *p* semi-core states were treated as valence states for Fe potentials in all calculations. Standard potentials were used for all other elements. The cutoff energy for a plane-wave expansion of 400 eV was used for adsorption calculations. We included on-site Coulomb interaction to treat the highly correlated Fe 3d-electrons in the framework of Dudarev et al. [43] using

an effective Hubbard energy of  $U = 3.7$  eV [44]. Colinear spin-polarized calculations were performed for all structures. Magnetic moments were initialized with opposing spin orientations of magnitude  $4.0 \mu_B$  for tetrahedrally and octahedrally coordinated Fe atoms [45]. Only forces were relaxed for surface models of  $\text{Fe}_3\text{O}_4$  with an additional constraint of atomic position for the middle three layers of the  $\text{Fe}_3\text{O}_4$  surface structure, to maintain bulk atomic positions. The structure was considered as optimized when the magnitude of Hellmann–Feynman forces acting on atoms dropped below  $50 \text{ meV } \text{\AA}^{-1}$  and components of the stress tensor did not exceed 1 kbar. The ground state energy was calculated using first-order Methfessel–Paxton smearing with a width of 0.02 eV. A blocked-Davidson algorithm with high precision is used during the relaxation of the bulk and surface  $\text{Fe}_3\text{O}_4$  structures. The Brillouin zone was sampled with a  $\Gamma$ -centered k-mesh generated automatically with a linear density of 30 divisions per  $1 \text{ \AA}^{-1}$  of the reciprocal space.

The electronic and charge properties of the murexide adsorbate and  $\text{Fe}_3\text{O}_4$  system were investigated by analyzing the Bader charge [46] and DOS analysis. In Bader analysis, the electron charge distribution from the DFT calculation was partitioned and assigned to individual atoms. The differences in the partitioned charge before and after adsorption indicate charge transfer between the surface and adsorbate. DOS analysis examines chemical bonding interactions by showing the changes in the occupation of the electron energy levels associated with adsorption. Charge density planar average and DOS plots were obtained from data using VASPKIT [47].

All structure files and VASP input files used in this work can be found in the Zenodo file repository [48]. Structure files can be visualized in VESTA [49].

## Results and discussion

### Experimental results

In this study, murexide was investigated as both a dispersing and capping agent to facilitate the co-dispersion of  $\text{Fe}_3\text{O}_4$  nanoparticles and CNTs to be used as the active material in supercapacitor anodes. Five techniques were conducted and tested where an electrode was fabricated from  $\text{Fe}_3\text{O}_4$  and CNTs with no additives (NA), 5% murexide added as a dispersing agent to synthesized  $\text{Fe}_3\text{O}_4$  particles and CNTs

in a solution of ethanol and dispersed in ethanol via probe ultrasonication (DE), 5% murexide added as a dispersing agent to synthesized  $\text{Fe}_3\text{O}_4$  particles and CNTs in a solution of water and dispersed water via probe ultrasonication (DW), 5% murexide as a capping agent added during synthesis of  $\text{Fe}_3\text{O}_4$  (C5), and 10% murexide as a capping agent added during synthesis of  $\text{Fe}_3\text{O}_4$  (C10). X-ray diffraction studies confirmed synthesis of spinel  $\text{Fe}_3\text{O}_4$  particles (Supplementary Information, Fig. S1). Transmission electron microscopy studies showed that the use of murexide as a capping agent resulted in particle size reduction (Fig. S2). Scanning electron microscopy investigations of the electrodes showed that the use of murexide as a capping agent facilitated the formation of electrodes with reduced agglomeration, improved mixing of  $\text{Fe}_3\text{O}_4$  and CNT and enhanced porosity (Fig. S3). Fourier transform infrared spectroscopy studies confirmed the adsorption of murexide on  $\text{Fe}_3\text{O}_4$  (Fig. S4). Electrodes with high active mass loading of  $40 \text{ mg cm}^{-2}$  were prepared. The high active mass loading is necessary for practical applications.

The cyclic voltammetry (CV) curves in Fig. 1 clearly show that the addition of murexide provides an increase in electrode performance compared to the case where no additive is used. In the cases where murexide is used as strictly a dispersing agent (DE and DW), we can see a slight increase in the peak capacitance of the electrodes from  $2.4 \text{ F cm}^{-2}$  for NA to  $2.6 \text{ F cm}^{-2}$  and  $3.0 \text{ F cm}^{-2}$  for DE and DW, respectively, at a scan rate of  $2 \text{ mV s}^{-1}$ . We see capacitance retention at increasing scan rate improving greatly for DE and DW, where capacitance at  $100 \text{ mV s}^{-1}$  is  $2.3 \text{ F cm}^{-2}$  and  $2.0 \text{ F cm}^{-2}$ , respectively, compared to  $0.9 \text{ F cm}^{-2}$  for NA. For C5 and C10, peak capacitance increases much more significantly, reaching a peak capacitance of  $4.5 \text{ F cm}^{-2}$  and  $4.2 \text{ F cm}^{-2}$ , respectively, at  $2 \text{ mV s}^{-1}$  scan rate. The improved capacitance retention is not seen for C5 as capacitance fades to  $1.9 \text{ F cm}^{-2}$  at  $100 \text{ mV s}^{-1}$ . When the concentration of murexide used as a capping agent increases from 5% to 10%, we see capacitance retention similar to DE and DW, where capacitance at  $100 \text{ mV s}^{-1}$  is reported at  $3.4 \text{ F cm}^{-2}$ .

We see a greater increase in the peak capacitance with murexide used as a capping agent compared to as a dispersing agent. We do, however, see better capacitance retention when murexide is used as a dispersing agent compared to a capping agent at a concentration of 5%.

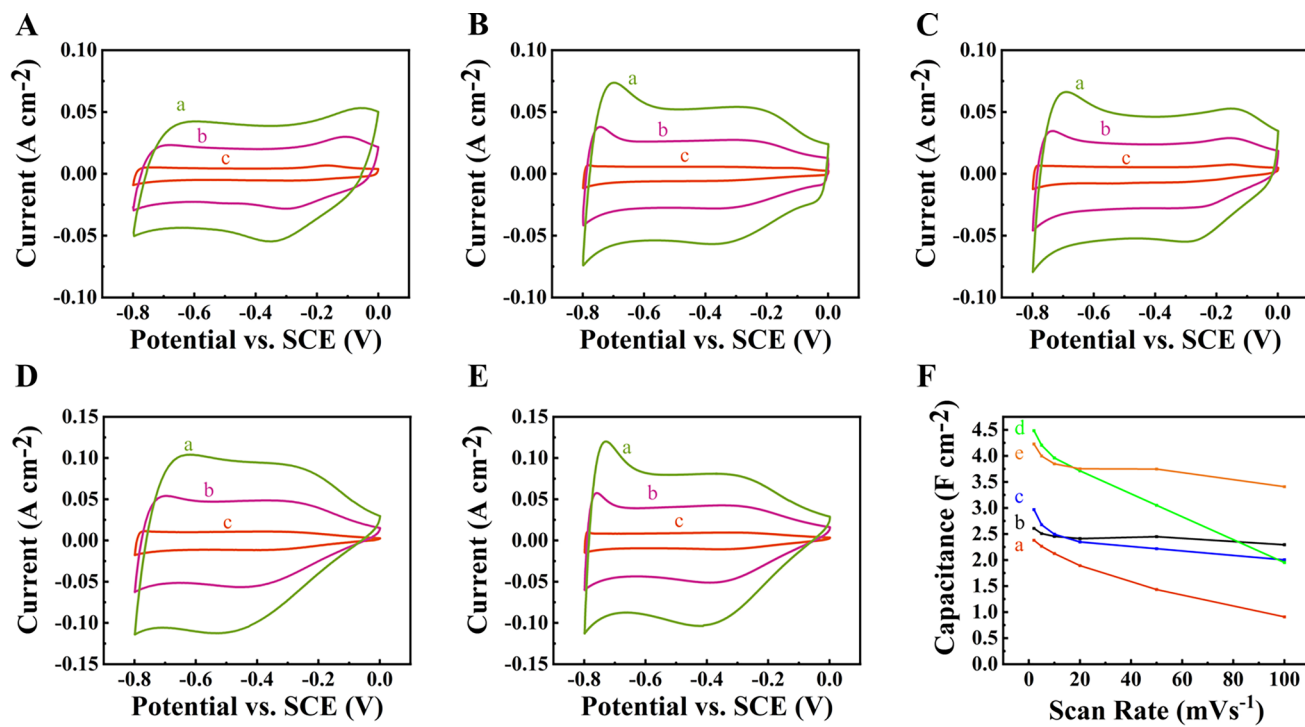


**Figure 1** A–E CVs at scan rates of (a) 20, (b) 10, and (c) 2  $\text{mV s}^{-1}$  for **A** NA, **B** DE, **C** DW, **D** C5, and **E** C10. **F** Capacitance versus scan rate for (a) NA, (b) DE, (c) DW, (d) C5, and (e) C10.

When synthesis of  $\text{Fe}_3\text{O}_4$  is conducted without additives, particles are able to agglomerate into larger particles after synthesis. Once murexide is introduced as a dispersing agent, these particles are no longer able to agglomerate further. This in combination with the adsorbed murexide playing the role of a charge transfer mediator results in a slight increase in peak capacitance and an improvement in the capacitance retention at higher scan rates.

It is known that increasing the scan rate can result in a decrease in the measured capacitance [50]. This is because the scan rate affects the amount of time that the electrochemical reactions have to take place at the electrode–electrolyte interface [51, 52]. This results in the resistance at the electrode–electrolyte interface becoming a limiting factor in the charging and discharging processes at high scan rates [51, 53]. Murexide shows redox active peaks in the negative potential range, leading to a reversible 1 electron transfer process [29] and allowing murexide to serve as a charge transfer mediator in a negative potential window. This charge transfer mediation allows for a decrease in resistance at the electrode–electrolyte interface. This means that electrons can more easily transfer during the surface redox reactions necessary for charge

storage, which at high scan rates, need to happen very quickly in order to retain capacitance.

As a capping agent during synthesis, murexide is able to form complexes with the actively forming  $\text{Fe}_3\text{O}_4$  surfaces. This prevents agglomeration as well as controls the growth of the  $\text{Fe}_3\text{O}_4$  particles during formation. This results in a suspension containing smaller particles, which allows for the fabrication of an electrode with a higher active surface area for the necessary surface redox reaction to take place during cycling.

When the concentration of murexide as a capping agent is increased from 5% to 10%, there is more murexide to facilitate charge transfer from electrolyte to the active electrode material, effectively decreasing resistance at the electrode–electrolyte interface due to the redox properties of murexide. The redox properties of murexide will contribute indirectly to the capacitance of the electrode. This is evident in the samples where murexide is used as a capping agent (Fig. 1D, E) where we see an increase in the CV area specifically in the more negative potential range. The increase in CV area in only this range can be attributed to the influence of the adsorbed murexide molecule, which exhibits redox peaks in this range.

Figure 2 compares the galvanostatic charge–discharge (GCD) curves (panels A–E) for different electrodes, with corresponding capacitance (panel F) calculated from the discharge data at different current densities. GCD was performed in a potential window of  $-0.8$  V to  $0$  V vs SCE. Nearly symmetrical and triangular charge–discharge curves are seen, confirming the pseudocapacitive behavior. Similar to the trends we see with the CV data, when electrodes showed only a slight increase in capacitance when murexide is used as a dispersing agent. For murexide as a dispersing agent in ethanol and water, we see a peak capacitance of  $2.8\text{ F cm}^{-2}$  and  $2.7\text{ F cm}^{-2}$ , respectively, at the current density of  $3\text{ mA cm}^{-2}$  compared to a value of  $2.4\text{ F cm}^{-2}$  for the case where no additive is used. When murexide is used as a capping agent, we again see a much more significant increase in the value of capacitance. For murexide as a capping agent with a concentration of  $5\%$  and  $10\%$ , we see a peak capacitance of  $4.6\text{ F cm}^{-2}$  and  $4.1\text{ F cm}^{-2}$ , respectively, at the current density of  $3\text{ mA cm}^{-2}$ . At current densities above  $10\text{ mA cm}^{-2}$ , we see that the capacitance of C10 exceeds that of C5.

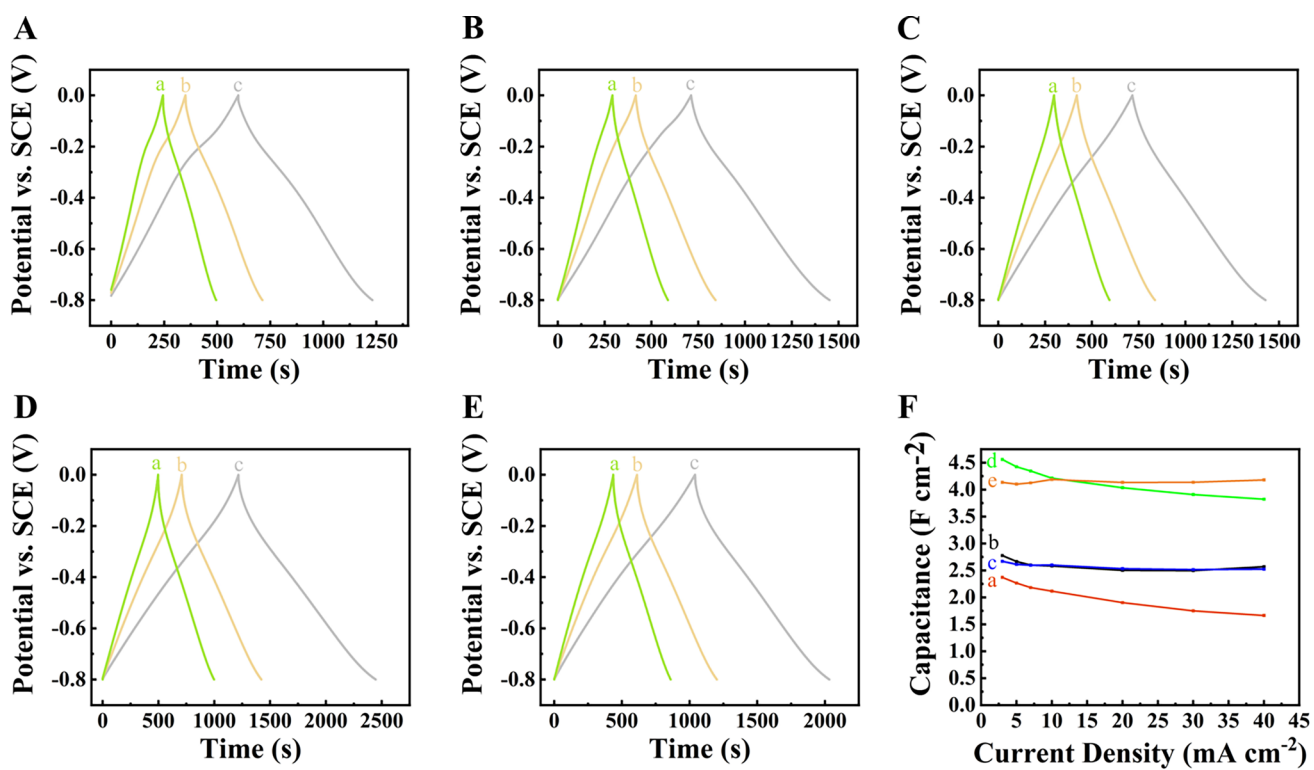


**Figure 2** **A–E** Charge–discharge curves at current densities of (a)  $7$ , (b)  $5$ , and (c)  $3\text{ mA cm}^{-2}$  for **A** NA, **B** DE, **C** DW, **D** C5, and **E** C10. **F** Capacitance versus current density profiles for (a) NA, (b) DE, (c) DW, (d) C5, and (e) C10.

The analysis of impedance data further provides evidence of the improved performance of the electrodes fabricated using murexide for surface modification of  $\text{Fe}_3\text{O}_4$ . In Fig. 3, we present the impedance at more negative potentials via Nyquist plots. We see a substantial decrease in the value of the real part of impedance for samples that were prepared with murexide, indicating that the presence of murexide results in easier charge transfer at more negative potentials. Although DE and DW samples exhibit the lowest real part of impedance at an electrode potential of  $0$  V versus SCE, we see that the C5 and C10 samples exhibit much lower impedance at more negative electrode potentials (below  $-0.2$  V versus SCE). This decrease in impedance at lower electrode potentials is explained by the redox and electron mediation properties of murexide in this potential range.

Figure 4 shows the real part of capacitance for each of the five electrodes at  $0$ ,  $-0.2$ ,  $-0.4$ ,  $-0.6$ , and  $-0.8$  V versus SCE. We see a significant improvement in the real part of capacitance ( $C'$ ) for the C5 and C10 samples at electrode potentials below  $-0.2$  V versus SCE compared to other samples. This is consistent with what we see in the CV data, where the area of the CV

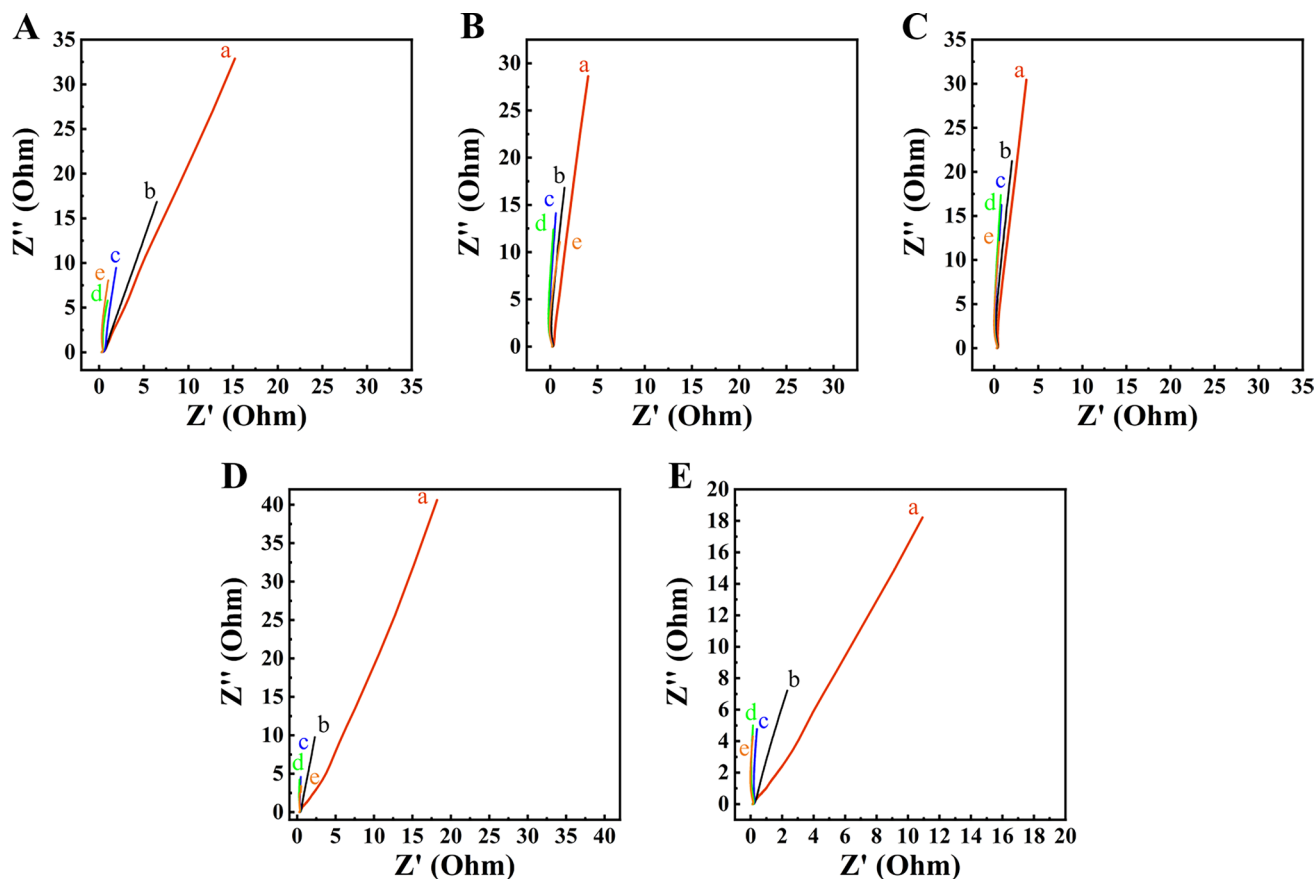


**Figure 3** Nyquist plots for **A** NA, **B** DE, **C** DW, **D** C5, and **E** C10 at electrode potentials of (a) 0, (b) –0.2, (c) –0.4, (d) –0.6, and (e) –0.8 V versus SCE.

curves drastically increases at lower electrode potentials when murexide is used as a capping agent. We see similar results with the dispersing agent samples (DE and DW) where the real part of capacitance is comparable to the case where no additive is used.

From Fig. 5, an increase of relaxation frequency from the imaginary part of impedance ( $C''$ ) for the electrodes prepared with murexide as a dispersing agent (DE and DW) is observed. With the analysis of impedance at more negative electrode potentials, we see an increase in both the real part of capacitance (Fig. 4) and the relaxation frequency (Fig. 5) for samples prepared with murexide, indicating the indirect contribution to the overall capacitance of the electrodes via the charge mediation properties of murexide. Additionally, the decrease observed in the real part of impedance (Fig. 3) indicates relatively low resistance and the large slope shown in the  $Z''$  versus  $Z'$  curves shows good capacitive behavior, especially at lower electrode potentials.

#### DFT modeling of murexide adsorption on $\text{Fe}_3\text{O}_4$ (001) surface

DFT modeling of the adsorption process of murexide on the surface of  $\text{Fe}_3\text{O}_4$  is conducted. The structural model (in the lowest energy configuration) is illustrated in Fig. 6. One hydrogen atom is cleaved from the murexide molecule and accommodated by  $\text{Fe}_3\text{O}_4$  to form a surface OH group. Relaxation of bulk cubic  $\text{Fe}_3\text{O}_4$  unit cell and subsequent construction of the (001) surface was performed following the procedure described elsewhere [54]. The selected stoichiometric surface terminated with tetrahedrally coordinated Fe atoms is in line with previous computational studies [55, 56] which have identified this (001) surface and its termination as the most energetically favorable.

Adsorption strength of murexide to the surface of  $\text{Fe}_3\text{O}_4$  is evaluated by the calculation of an adsorption enthalpy ( $H_{\text{ads}}$ ), which represents the difference

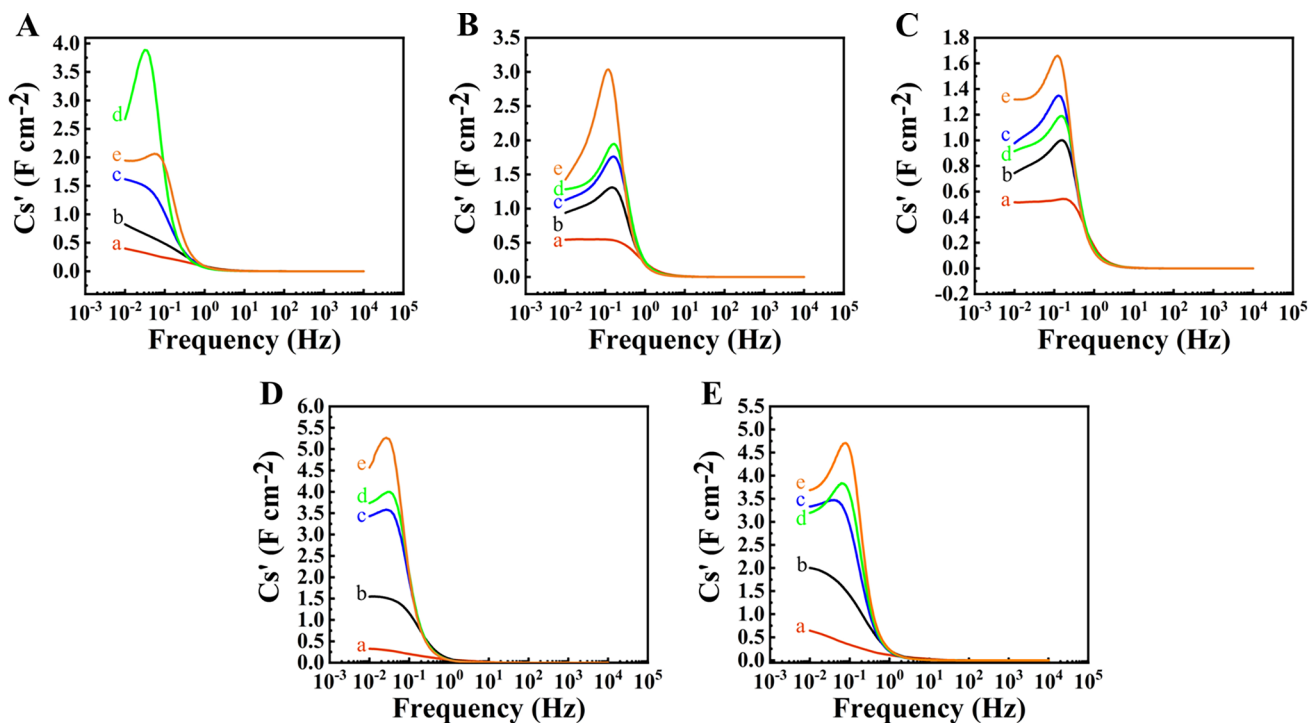


**Figure 4** Real part of capacitance ( $C'$ ) plots for **A** NA, **B** DE, **C** DW, **D** C5, and **E** C10 at electrode potentials of (a) 0, (b) -0.2, (c) -0.4, (d) -0.6, and (e) -0.8 V versus SCE.

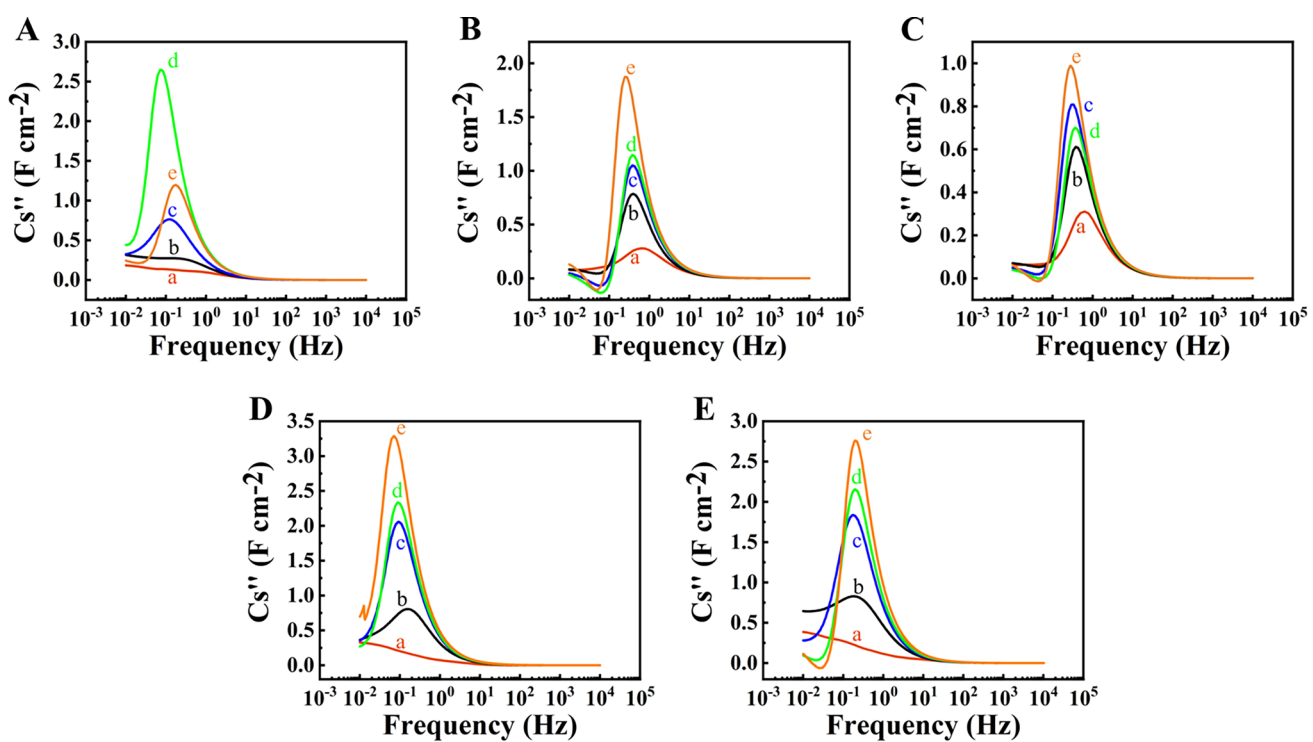


**Figure 5** Imaginary part of capacitance ( $C''$ ) plots for **A** NA, **B** DE, **C** DW, **D** C5, and **E** C10 at electrode potentials of (a) 0, (b) -0.2, (c) -0.4, (d) -0.6, and (e) -0.8 V versus SCE.

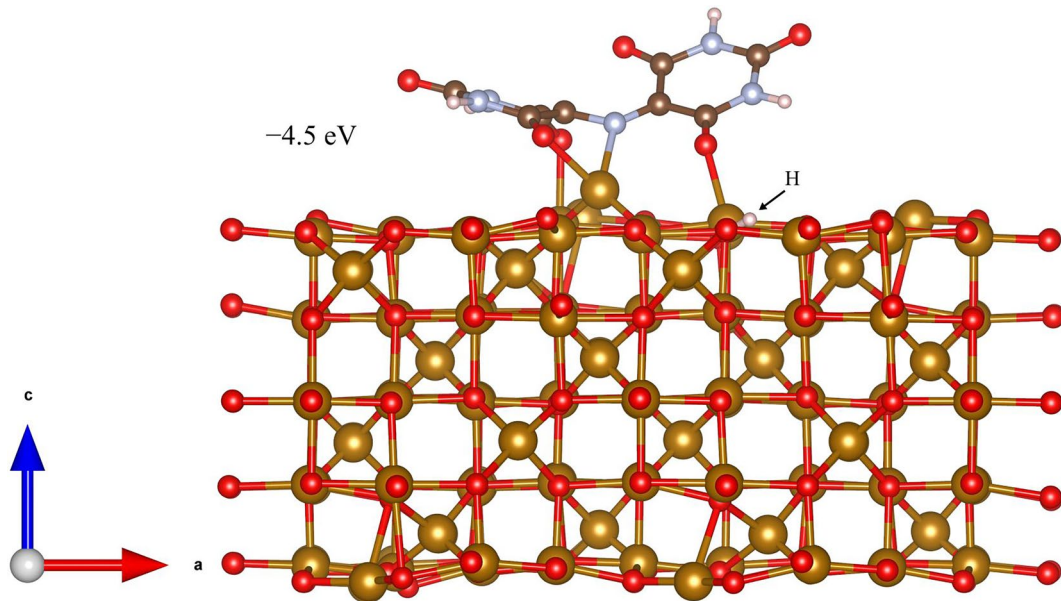


**Figure 6** Adsorption of murexide on the (001) surface of  $\text{Fe}_3\text{O}_4$ . The adsorption is accompanied by the surface adsorption of an  $\text{H}^+$  ion displaced from the  $\text{OH}$  group on the murexide molecule. The value of adsorption enthalpy is indicated.

between the total energy ( $E_{\text{tot}}$ ) of the adsorbed and desorbed states

$$H_{\text{ads}} = H_{\text{tot}}^{\text{ads}} - H_{\text{tot}}^{\text{des}}. \quad (1)$$

The desorbed state is modeled as the surface slab with the murexide molecule positioned 10 Å above the surface in the vacuum layer. Our calculations yield an enthalpy of  $H_{\text{ads}} = -4.5$  eV. This value indicates very strong adsorption, consistent with previous studies reporting adsorption enthalpies ranging from  $-1.8$  eV for other organic molecules [54] to  $-5.5$  eV for adsorption of single adatoms [44, 56] on the  $\text{Fe}_3\text{O}_4$  (001) surface. In comparison with other organic molecules, the adsorption enthalpy of murexide onto the surface of  $\text{Fe}_3\text{O}_4$  exhibits a remarkable increase, attributed to the formation of four bonds with the surface. This significant enhancement in adsorption energy can be attributed to the unique bonding mechanism of murexide, which involves the simultaneous formation of both bridging and chelating bonds. The adsorption of murexide results in bonding to surface Fe atoms in a manner that maintains the octahedral or tetrahedral coordination, and distorts the surface to result in coordination of surface Fe atoms closer to that of the bulk Fe atoms in the  $\text{Fe}_3\text{O}_4$ .

In addition to the calculation of adsorption energies, the adsorption mechanism is also investigated

using charge density difference plots and Bader charge analysis. Figure 7B presents the three-dimensional charge density difference where the charge density of the separate surface ( $\rho_{\text{surf}}$ ) and molecule, which includes the accommodated H, ( $\rho_{\text{mol}}$ ) is subtracted from the charge density of the adsorbed molecule on the  $\text{Fe}_3\text{O}_4$  surface ( $\rho_{\text{ads}}$ )

$$\Delta\rho = \rho_{\text{ads}} - \rho_{\text{surf}} - \rho_{\text{mol}}. \quad (2)$$

Figure 7A plots the charge density planar average along the z-direction where the panel (C) plots the amount of charge transferred up to  $z$ , and is given by

$$\Delta Q(z) = \int_0^z \Delta\rho(z) dz. \quad (3)$$

From Fig. 7A, we can see that the charge density around the  $\text{Fe}_3\text{O}_4$  surface changes from positive to negative, indicating a transfer of negative charge from the  $\text{Fe}_3\text{O}_4$  surface to the murexide molecule. From panel (C), we see that the largest magnitude of charge transfer occurs at  $z = 13$  Å, which is in the region where the bonds are formed between murexide and the  $\text{Fe}_3\text{O}_4$  surface during adsorption. The total net number of electrons transferred between the  $\text{Fe}_3\text{O}_4$  surface and adsorbed murexide is 0.79 e, which implies an electron deficiency in the  $\text{Fe}_3\text{O}_4$  slab due to the adsorbed murexide molecule.

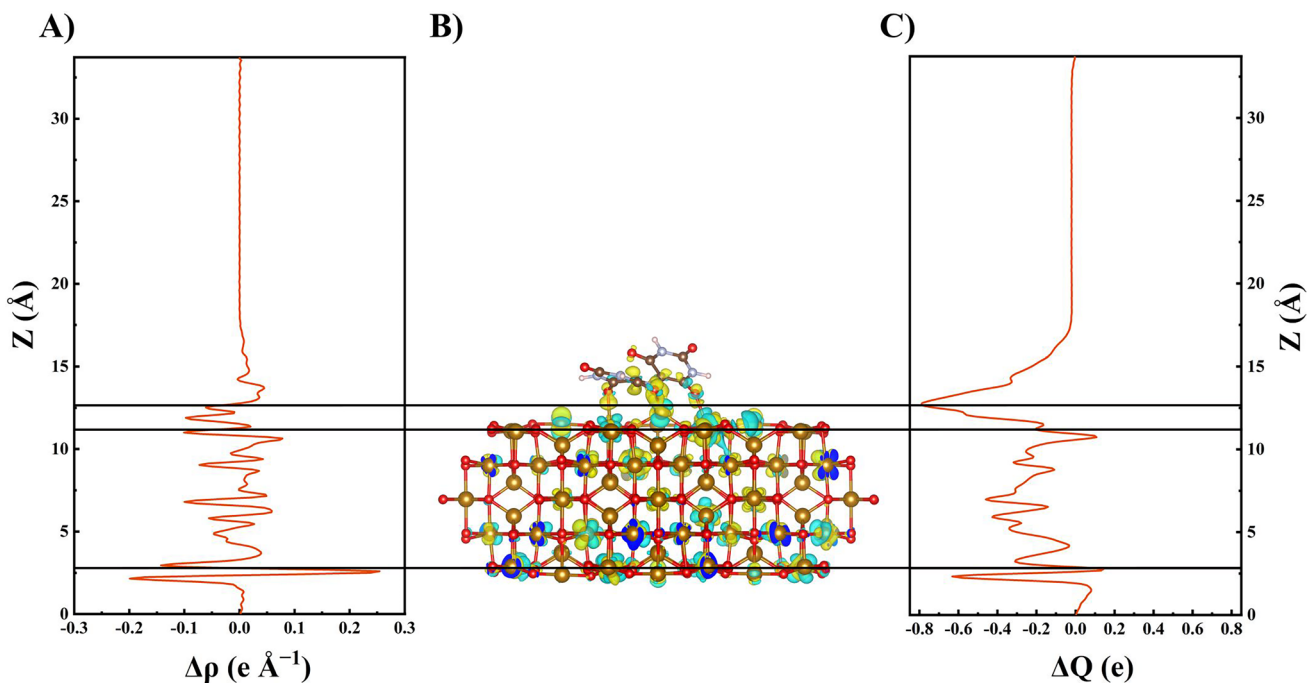


**Figure 7** A Charge density difference planar average of murexide adsorbed on  $\text{Fe}_3\text{O}_4$  surface, plotted along the  $z$ -axis, B schematic of adsorbed murexide on  $\text{Fe}_3\text{O}_4$  with three-dimensional isosurface of the charge density difference (rendered value of

$\pm 0.0065 \text{ e } \text{\AA}^{-3}$ ), where yellow region represents area of electron accumulation and blue region represents area of electron depletion during the adsorption process, and C integral charge transfer  $\Delta Q(z)$  with respect to position along the  $z$ -axis.

Since the charge density planar average is an average of the charge density at each point along the  $z$ -axis, we use Bader charge analysis [46, 57] to further investigate the charge transfer between  $\text{Fe}_3\text{O}_4$  and murexide during adsorption on an atom-by-atom basis. The

Bader charges are shown in Table 1, where we list the difference in Bader net atomic charges between the adsorbed molecule on  $\text{Fe}_3\text{O}_4$  and the separate  $\text{Fe}_3\text{O}_4$  surface and molecule. The bonds between murexide and  $\text{Fe}_3\text{O}_4$  are shown in Fig. 8 from the

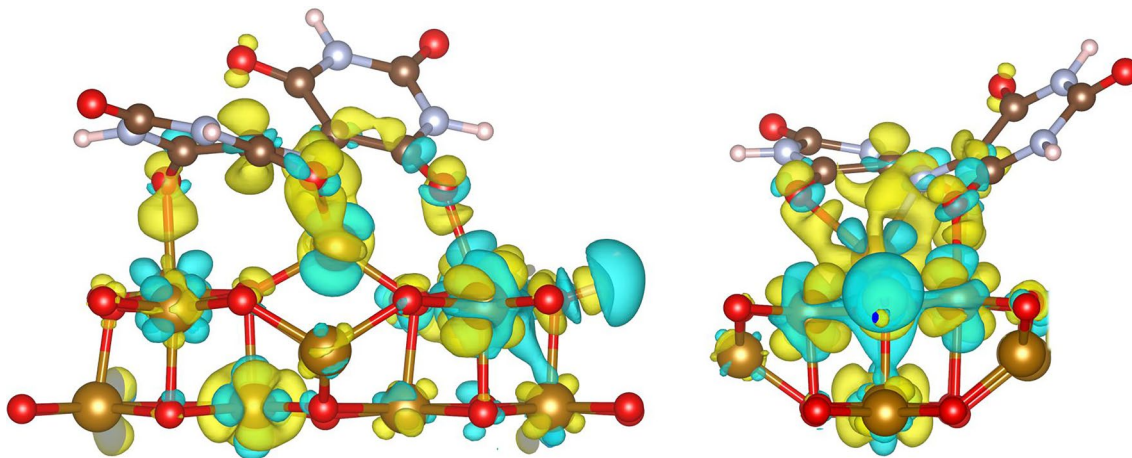


**Figure 8** Close-up view of three-dimensional isosurface of the charge density difference (rendered value of  $\pm 0.0065 \text{ e } \text{\AA}^{-3}$ ) for atoms involved in murexide bonding to  $\text{Fe}_3\text{O}_4$  surface, where

yellow region represents area of electron accumulation and blue region represents area of electron depletion during the adsorption process.

**Table 1** Bader charge (in units of  $|e|$ ) of selected atoms associated with murexide adsorption (see Fig. 9 for labels)

Location	Separate	Bonded	Difference
Surface			
Fe <sub>1</sub>	1.58	1.73	0.15
Fe <sub>2</sub>	1.33	1.66	0.33
Fe <sub>3</sub>	1.58	1.70	0.12
Sum	—	—	0.60
Murexide			
O <sub>1</sub>	−1.00	−1.17	−0.17
O <sub>2</sub>	−0.98	−1.10	−0.12
O <sub>3</sub>	−1.04	−1.15	−0.11
N	−0.95	−1.17	−0.22
Sum	—	—	−0.62

three-dimensional isosurface of charge density difference before and after adsorption. It is clear that electron accumulation occurs on the atoms involved in bonding that are part of the murexide molecule, where they are depleted from the surface Fe atoms, shown by the yellow and blue surfaces, respectively. This formation of a dipole results in the ionic nature of bonding of murexide onto the  $\text{Fe}_3\text{O}_4$  surface.

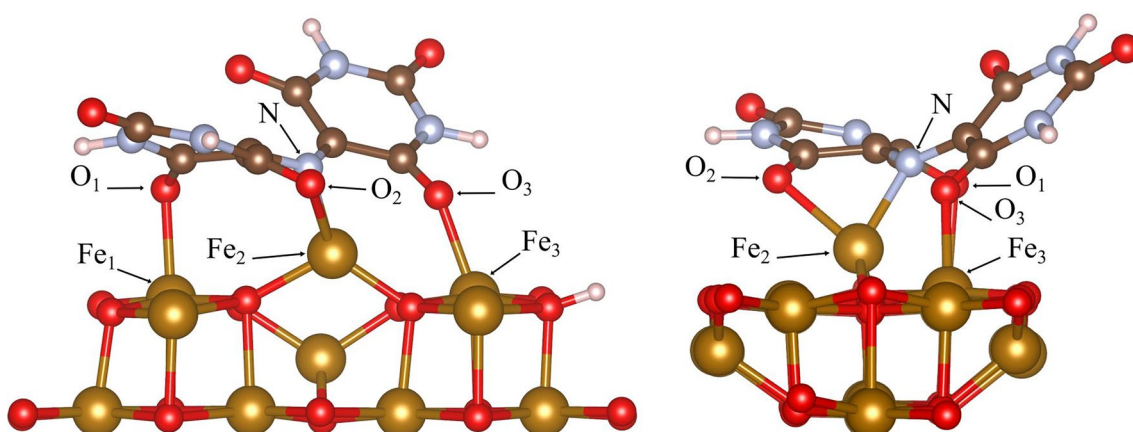
By investigating the Bader charge difference between atoms in the adsorbed and desorbed states, we can gain insight into the charge transfer that occurs during the adsorption process, and which specific atoms play a role. From Bader charge analysis (Table 1), during the adsorption of murexide onto the  $\text{Fe}_3\text{O}_4$  surface, we see a decrease in the Bader charge of 0.60 for the murexide molecule with a subsequent increase of 0.62 for the  $\text{Fe}_3\text{O}_4$  surface. This indicates

a depletion of electrons from the  $\text{Fe}_3\text{O}_4$  surface with accumulation occurring in the murexide molecule. We can see this charge transfer takes place directly at the adsorption sites, where the bonds between the atoms in the murexide molecule form with the Fe atoms in the  $\text{Fe}_3\text{O}_4$  surface.

From the charge density difference and Bader charge analysis, we can clearly see that the transfer of electrons from the  $\text{Fe}_3\text{O}_4$  surface to murexide plays a critical role in the adsorption of murexide on  $\text{Fe}_3\text{O}_4$ . Additionally, this pathway for electron transfer may provide insight into the charge transfer mediation that murexide provides in  $\text{Fe}_3\text{O}_4$  supercapacitor anodes at negative electrode potentials.

From Fig. 10, we can see that, for both spins, the lowest unoccupied molecular orbital (LUMO) and the highest occupied molecular orbital (HOMO) of the murexide molecule are positioned lower in energy compared to the conduction band edge (CBE) and valence band edge (VBE) of the  $\text{Fe}_3\text{O}_4$ , respectively. This energetic arrangement plays a pivotal role in electron transfer dynamics during the adsorption process. Specifically, the lower energy positioning of the murexide's LUMO facilitates the acceptance of electrons from the  $\text{Fe}_3\text{O}_4$  conduction band, enabling efficient charge transfer from the metal oxide surface to the adsorbed molecule. This energetic alignment may also promote enhanced electron transfer efficiency, with the possibility to increase the overall conductivity and performance of the system.

Further investigation of the density of states (DOS) reveals the formation of a band gap after the adsorption of murexide, while the surface is metallic

**Figure 9** Close-up view of murexide adsorbed onto  $\text{Fe}_3\text{O}_4$  surface with atoms labeled for Bader charge analysis.

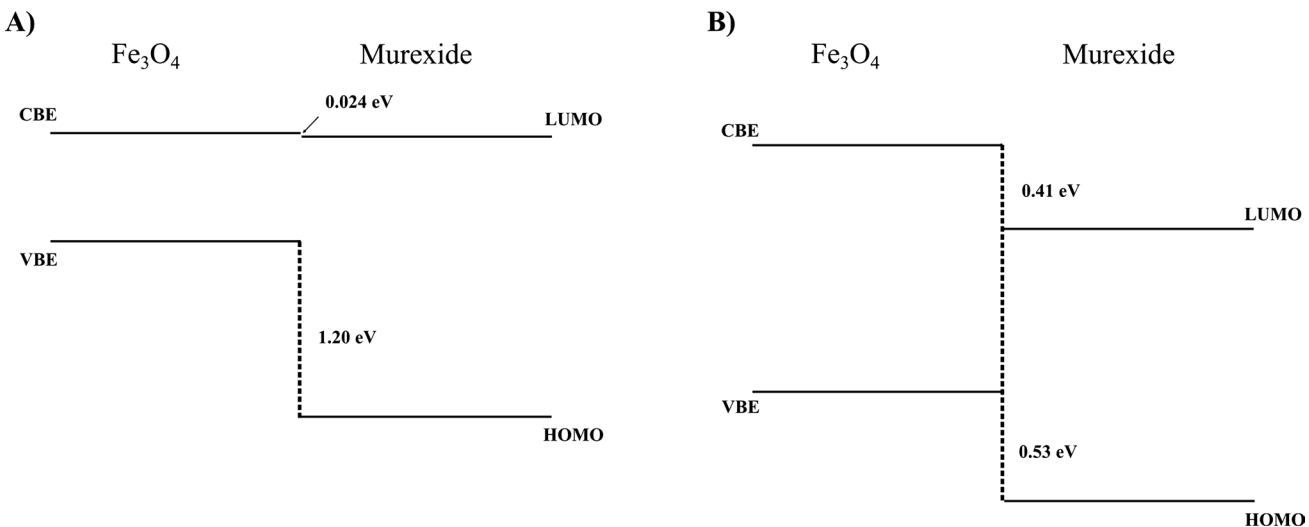


**Figure 10** Schematic energy band alignment for **A** spin up and **B** spin down electronic states at the interface  $\text{Fe}_3\text{O}_4$ /murexide.

(for one of the spin channels) in the non-adsorbed state (Fig. 11). This band gap formation is shown in Fig. 11, where the density of states for the  $\text{Fe}_3\text{O}_4$  surface before (A) and after (B) adsorption is shown. The formation of a band gap after murexide adsorption suggests a change in the electronic structure of the system. Adsorption-induced modifications, such

as charge redistribution, can open up a band gap in the energy spectrum [58]. From charge density and Bader charge analysis, the adsorption of murexide molecule on the  $\text{Fe}_3\text{O}_4$  surface leads to a redistribution of charge. We see that the interaction between the murexide molecule and the surface atoms results

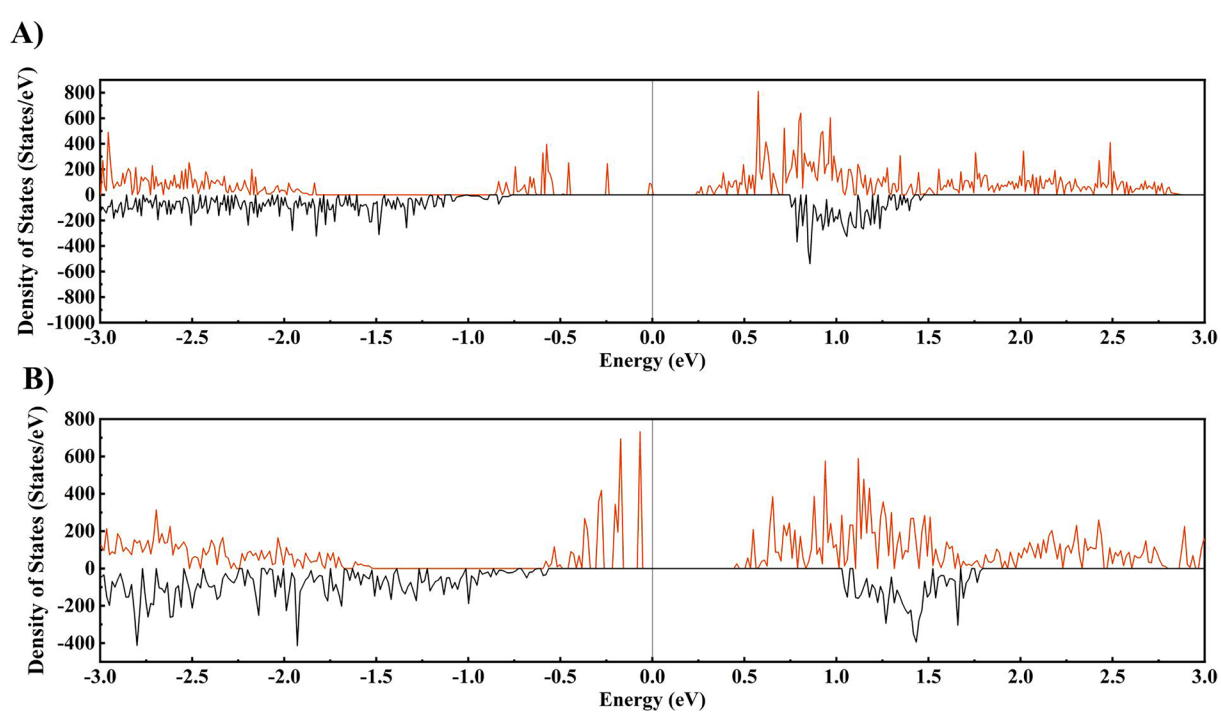


**Figure 11** Density of states of the  $\text{Fe}_3\text{O}_4$  surface before (A) and after (B) adsorption of murexide, where the red and black curves represent spin up and spin down, respectively. The Fermi energy is normalized to 0 eV.

in charge transfer, which can alter the occupancy of electronic states near the Fermi level.

## Conclusion

In conclusion, the experimental results presented in this study provide evidence for the effectiveness of murexide as a capping agent to enhance the performance of MWCNT- $\text{Fe}_3\text{O}_4$  supercapacitor anodes. The addition of murexide, whether as a dispersing agent or a capping agent, resulted in significant improvements in electrode performance compared to the case without any additive. When used as a dispersing agent, 5% murexide in ethanol and water led to slight increases in peak capacitance and remarkable improvements in capacitance retention at higher scan rates. On the other hand, murexide as a capping agent during synthesis resulted in a more substantial, 1.9-fold increase in peak capacitance, reaching values as high as  $4.6 \text{ F cm}^{-2}$  in the case of the C5 sample, and maintaining the improved capacitance retention when murexide concentration is increased.

The analysis of impedance data further supported the enhanced performance of murexide-modified electrodes, showing easier charge transfer and improved capacitance at negative electrode potentials. GCD data confirmed the pseudocapacitive behavior of the electrodes and demonstrated the superior charge storage capacity of murexide-modified electrodes. Murexide facilitated charge transfer and acted as a charge transfer mediator.

The atomistic modeling of the adsorption process of murexide on the  $\text{Fe}_3\text{O}_4$  surface provided valuable insights into the adsorption strength, bonding characteristics, charge transfer, and electronic properties. The strong adsorption of murexide on the  $\text{Fe}_3\text{O}_4$  surface is indicated by an adsorption enthalpy of  $-4.5 \text{ eV}$ . Additionally, it is evident that the coordination of Fe atoms in bonding significantly influences the interaction between atoms. Specifically, O and N from murexide forms bonds with surface Fe atoms in a manner which restores their respective bulk tetrahedral or octahedral coordination. Further analysis using charge density difference plots, Bader charge analysis, and DOS demonstrated the transfer of electrons from the  $\text{Fe}_3\text{O}_4$  surface to murexide and was found to play a critical role in the adsorption process. This electron transfer pathway may have implications for the charge transfer mediation provided by

murexide in  $\text{Fe}_3\text{O}_4$  supercapacitor anodes at negative electrode potentials. Additionally, the band alignment analysis reveals that the lower energy levels of the LUMO and HOMO of the murexide molecule compared to the CBE and VBE of  $\text{Fe}_3\text{O}_4$ , respectively, allows for the transfer of electrons from the  $\text{Fe}_3\text{O}_4$  surface to murexide during adsorption, and may illustrate a conductive pathway for electrons to decrease electrode resistance.

Overall, these findings contribute to a deeper understanding of the interaction between murexide and  $\text{Fe}_3\text{O}_4$  and have implications for the development of advanced energy storage systems. The demonstrated improvements in electrode performance and the insights into the adsorption process and charge transfer mechanisms provide a foundation for further exploration of murexide and its potential applications in various fields, including energy storage devices.

*Note added during review* The following references were added to provide more information for the broader readers [59–61].

## Supplementary information

Supplementary Information contains X-ray diffraction, transmission electron microscopy, scanning electron microscopy, and Fourier transform infrared spectroscopy data. References cited within the supplementary information section only [62–66].

## Acknowledgements

This research was funded by the Natural Sciences and Engineering Research Council of Canada, grant number RGPIN-2018-04014, and Faculty of Engineering of McMaster University. Calculations were performed using the Compute Canada infrastructure supported by the Canada Foundation for Innovation under John R. Evans Leaders Fund.

## Author contributions

Conceptualization was prepared by I.Z. and C.B.; carrying out experiments and calculations and writing original draft were done by C.B. and D.T.; data

analysis and interpretation were revised by C.B., D.T., I.Z., and O.R.; manuscript review and editing were analyzed by I.Z. and O.R..

## Data availability

The raw data (VASP input and structure files) required to reproduce computational findings are available in the Zenodo file repository [48].

## Declarations

**Conflict of interest** There are no conflicts of interest exist.

**Supplementary Information** The online version contains supplementary material available at <https://doi.org/10.1007/s10853-024-09524-5>.

## References

- [1] Olabi AG, Abbas Q, Al Makky A, Abdelkareem MA (2022) Supercapacitors as next generation energy storage devices: properties and applications. *Energy* 248(123617):123617. <https://doi.org/10.1016/j.energy.2022.123617>
- [2] Forouzandeh P, Kumaravel V, Pillai SC (2020) Electrode materials for supercapacitors: a review of recent advances. *Catalysts* 10(9):969. <https://doi.org/10.3390/catal10090969>
- [3] Silva RME, Poon R, Milne J, Syed A, Zhitomirsky I (2018) New developments in liquid-liquid extraction, surface modification and agglomerate-free processing of inorganic particles. *Adv Colloid Interface Sci* 261:15–27. <https://doi.org/10.1016/j.cis.2018.09.005>
- [4] Zhao Q, Wang X, Liu J, Wang H, Zhang Y, Gao J, Liu J, Lu Q (2015) Surface modification and performance enhancement of carbon derived from chromium carbide for supercapacitor applications. *J Electrochem Soc* 162(6):845–851. <https://doi.org/10.1149/2.0331506jes>
- [5] Pimsawat A, Tangtrakarn A, Pimsawat N, Daengsakul S (2019) Effect of substrate surface roughening on the capacitance and cycling stability of  $\text{Ni(OH)}_2$  nanoarray films. *Sci Rep* 9(1):16877. <https://doi.org/10.1038/s41598-019-53365-1>
- [6] Yang LW, Zhitomirsky I (2023) Influence of capping agents on the synthesis of  $\text{Mn}_3\text{O}_4$  nanostructures for supercapacitors. *ACS Appl Nano Mater* 6(6):4428–4436. <https://doi.org/10.1021/acsanm.2c05519>
- [7] Chen W, Rakhi RB, Hu L, Xie X, Cui Y, Alshareef HN (2011) High-performance nanostructured supercapacitors on a sponge. *Nano Lett* 11(12):5165–5172. <https://doi.org/10.1021/nl2023433>
- [8] Shao Y, El-Kady MF, Sun J, Li Y, Zhang Q, Zhu M, Wang H, Dunn B, Kaner RB (2018) Design and mechanisms of asymmetric supercapacitors. *Chem Rev* 118(18):9233–9280. <https://doi.org/10.1021/acs.chemrev.8b00252>
- [9] Brousse T, Bélanger D (2003) A hybrid  $\text{Fe}_3\text{O}_4\text{-MnO}_2$  capacitor in mild aqueous electrolyte. *Electrochim Solid State Lett* 6(11):A244–A248. <https://doi.org/10.1149/1.1614451>
- [10] Gogotsi Y, Simon P (2011) True performance metrics in electrochemical energy storage. *Science* 334(6058):917–918. <https://doi.org/10.1126/science.1213003>
- [11] Ata MS, Liu Y, Zhitomirsky I (2014) A review of new methods of surface chemical modification, dispersion and electrophoretic deposition of metal oxide particles. *RSC Adv* 4(43):22716–22732. <https://doi.org/10.1039/C4RA02218A>
- [12] Yang W, Nawwar M, Zhitomirsky I (2022) Facile route for fabrication of ferrimagnetic  $\text{Mn}_3\text{O}_4$  spinel material for supercapacitors with enhanced capacitance. *Energies* 15(5):1812. <https://doi.org/10.3390/en15051812>
- [13] Ata MS, Zhitomirsky I (2012) Electrophoretic nanotechnology of ceramic films. *Adv Appl Ceram* 111(5–6):345–350. <https://doi.org/10.1179/174367611y.0000000070>
- [14] Gulley-Stahl H, Hogan PA, Schmidt WL, Wall SJ, Buhrlage A, Bullen HA (2010) Surface complexation of catechol to metal oxides: an ATR-FTIR, adsorption, and dissolution study. *Environ Sci Technol* 44(11):4116–4121. <https://doi.org/10.1021/es902040u>
- [15] Liu Y, Zhitomirsky I (2014) Aqueous electrostatic dispersion and heterocoagulation of multiwalled carbon nanotubes and manganese dioxide for the fabrication of supercapacitor electrodes and devices. *RSC Adv* 4(85):45481–45489. <https://doi.org/10.1039/c4ra05879h>
- [16] Saiz-Poseu J, Mancebo-Aracil J, Nador F, Busqué F, Ruiz-Molina D (2018) The chemistry behind catechol-based adhesion. *Angew Chem Int Ed* 58(3):696–714. <https://doi.org/10.1002/anie.201801063>
- [17] Sakib S, Bakhshandeh F, Saha S, Soleymani L, Zhitomirsky I (2021) Surface functionalization of metal oxide semiconductors with catechol ligands for enhancing their photoactivity. *Sol RRL* 5(10):2100512. <https://doi.org/10.1002/solr.202100512>
- [18] Nawwar M, Poon R, Sahu RP, Puri IK, Zhitomirsky I (2020)  $\text{Fe}_3\text{O}_4$  spinel- $\text{Mn}_3\text{O}_4$  spinel supercapacitor prepared

- using celestine blue as a dispersant, capping agent and charge transfer mediator. *Ceram Int* 46(11):18851–18858. <https://doi.org/10.1016/j.ceramint.2020.04.204>
- [19] Yu H, Wu J, Fan L, Hao S, Lin J, Huang M (2014) An efficient redox-mediated organic electrolyte for high-energy supercapacitor. *J Power Sources* 248:1123–1126. <https://doi.org/10.1016/j.jpowsour.2013.10.040>
- [20] Yin Y, Zhou J, Mansour AN, Zhou X (2011) Effect of NaI/I<sub>2</sub> mediators on properties of PEO/LiAlO<sub>2</sub> based all-solid-state supercapacitors. *J Power Sources* 196(14):5997–6002. <https://doi.org/10.1016/j.jpowsour.2011.02.079>
- [21] Akinwolemiwa B, Peng C, Chen GZ (2015) Redox electrolytes in supercapacitors. *J Electrochem Soc* 162(5):5054–5059. <https://doi.org/10.1149/2.0111505jes>
- [22] Tamirat AG, Guan X, Liu J, Luo J, Xia Y (2020) Redox mediators as charge agents for changing electrochemical reactions. *Chem Soc Rev* 49(20):7454–7478. <https://doi.org/10.1039/D0CS00489H>
- [23] Roldán S, Blanco C, Granda M, Menéndez R, Santamaría R (2011) Towards a further generation of high-energy carbon-based capacitors by using redox-active electrolytes. *Angew Chem Int Ed Engl* 50(7):1699–1701. <https://doi.org/10.1002/anie.201006811>
- [24] Kashanian S, Gholivand MB, Madaeni S, Nikrahi A, Shamsipur M (1988) Spectrophotometric study of the complexation reactions between alkaline earth cations and murexide in some non-aqueous solutions. *Polyhedron* 7(14):1227–1230. [https://doi.org/10.1016/S0277-5387\(00\)81216-4](https://doi.org/10.1016/S0277-5387(00)81216-4)
- [25] Shamsipur M, Esmaili A, Amini MK (1989) Formation of cobalt, nickel and copper complexes with murexide in ethanol-water mixtures. *Talanta* 36(12):1300–1302. [https://doi.org/10.1016/0039-9140\(89\)80067-0](https://doi.org/10.1016/0039-9140(89)80067-0)
- [26] Shamsipur M, Madaeni S, Kashanian S (1989) Spectrophotometric study of the alkali metal-murexide complexes in some non-aqueous solutions. *Talanta* 36(7):773–776. [https://doi.org/10.1016/0039-9140\(89\)80147-x](https://doi.org/10.1016/0039-9140(89)80147-x)
- [27] Parham H, Shamsipur M (1992) Spectrophotometric study of some alkali and alkaline earth cryptates in dimethylformamide solution using murexide as a metallochromic indicator. *Polyhedron* 11(8):987–991. [https://doi.org/10.1016/S0277-5387\(00\)83352-5](https://doi.org/10.1016/S0277-5387(00)83352-5)
- [28] Masoud MS, Kassem TS, Shaker MA, Ali AE (2006) Studies on transition metal murexide complexes. *J Therm Anal Calorim* 84(3):549–555. <https://doi.org/10.1007/s10973-005-9991-3>
- [29] Mohran HS (2009) An electrochemical investigation of the redox properties of murexide in aqueous and non-aqueous media. *Am J Appl Sci* 6(5):964–969. <https://doi.org/10.3844/ajassp.2009.964.969>
- [30] Serwar M, Rana UA, Siddiqi HM, Ud-Din Khan S, Ahmed Ali FA, Al-Fatesh A, Adomkevicius A, Coca-Clemente JA, Cabo-Fernandez L, Braga F, Hardwick LJ (2017) Template-free synthesis of nitrogen doped carbon materials from an organic ionic dye (murexide) for supercapacitor application. *RSC Adv* 7:54626–54637. <https://doi.org/10.1039/C7RA10954G>
- [31] Atay NZ, Varnali T (2002) A semi-empirical study on metal ion/murexide complexation. *Turk J Chem* 26:303–310
- [32] Nawwar M, Poon R, Chen R, Sahu RP, Puri IK, Zhitomirsky I (2019) High areal capacitance of Fe<sub>3</sub>O<sub>4</sub>-decorated carbon nanotubes for supercapacitor electrodes. *Carbon Energy* 1(1):124–133. <https://doi.org/10.1002/cey.2.6>
- [33] Shi K, Zhitomirsky I (2013) Electrophoretic nanotechnology of graphene-carbon nanotube and graphene-polypyrrole nanofiber composites for electrochemical supercapacitors. *J Colloid Interface Sci* 407:474–481. <https://doi.org/10.1016/j.jmat.2018.02.004>
- [34] Zhu Y, Shi K, Zhitomirsky I (2014) Polypyrrole coated carbon nanotubes for supercapacitor devices with enhanced electrochemical performance. *J Power Sources* 268:233–239. <https://doi.org/10.1016/j.acsomega.9b04029>
- [35] Kohn W, Sham LJ (1965) Self-consistent equations including exchange and correlation effects. *Phys Rev* 140(4A):1133–1138. <https://doi.org/10.1103/PhysRev.140.A1133>
- [36] Perdew JP, Burke K, Ernzerhof M (1996) Generalized gradient approximation made simple. *Phys Rev Lett* 77(18):3865–3868. <https://doi.org/10.1103/PhysRevLett.77.3865>
- [37] Grimme S, Ehrlich S, Goerigk L (2011) Effect of the damping function in dispersion corrected density functional theory. *J Comput Chem* 32(7):1456–1465. <https://doi.org/10.1002/jcc.21759>
- [38] Grimme S, Antony J, Ehrlich S, Krieg H (2010) A consistent and accurate ab initio parametrization of density functional dispersion correction (DFT-D) for the 94 elements H–Pu. *J Chem Phys* 132(15):154104. <https://doi.org/10.1063/1.3382344>
- [39] Kresse G, Hafner J (1993) Ab initio molecular dynamics for liquid metals. *Phys Rev B* 47(1):558–561. <https://doi.org/10.1103/PhysRevB.47.558>
- [40] Kresse G, Furthmüller J (1996) Efficiency of ab-initio total energy calculations for metals and semiconductors using a plane-wave basis set. *Comput Mater Sci* 6(1):15–50. [https://doi.org/10.1016/0927-0256\(96\)00008-0](https://doi.org/10.1016/0927-0256(96)00008-0)
- [41] Kresse G, Furthmüller J (1996) Efficient iterative schemes for ab initio total-energy calculations using a plane-wave basis set. *Phys Rev B* 54(16):11169–11186. <https://doi.org/10.1103/PhysRevB.54.11169>

- [42] Kresse G, Joubert D (1999) From ultrasoft pseudopotentials to the projector augmented-wave method. *Phys Rev B* 59(3):1758–1775. <https://doi.org/10.1103/PhysRevB.59.1758>
- [43] Dudarev SL, Botton GA, Savrasov SY, Humphreys CJ, Sutton AP (1998) Electron-energy-loss spectra and the structural stability of nickel oxide: an LSDA+U study. *Phys Rev B* 57(3):1505–1509. <https://doi.org/10.1103/PhysRevB.57.1505>
- [44] Bliem R, Pavelec J, Gamba O, McDermott E, Wang Z, Gerhold S, Wagner M, Osiecki J, Schulte K, Schmid M, Blaha P, Diebold U, Parkinson GS (2015) Adsorption and incorporation of transition metals at the magnetite  $\text{Fe}_3\text{O}_4$  (001) surface. *Phys Rev B* 92(7):075440. <https://doi.org/10.1103/PhysRevB.92.075440>
- [45] Chiter F, Nguyen VB, Tarrat N, Benoit M, Tang H, Lacaze-Dufaure C (2016) Effect of van der Waals corrections on DFT-computed metallic surface properties. *Mater Res Express* 3(4):046501. <https://doi.org/10.1088/2053-1591/3/4/046501>
- [46] Henkelman G, Arnaldsson A, Jónsson H (2006) A fast and robust algorithm for Bader decomposition of charge density. *Comput Mater Sci* 36(3):354–360. <https://doi.org/10.1016/j.commatsci.2005.04.010>
- [47] Wang V, Xu N, Liu J-C, Tang G, Geng W-T (2021) VASP-KIT: a user-friendly interface facilitating high-throughput computing and analysis using VASP code. *Comput Phys Commun* 267:108033. <https://doi.org/10.1016/j.cpc.2021.108033>
- [48] Boucher C, Zhitomirsky I, Rubel O (2023) Application of murexide as a capping agent for fabrication of magnetite anodes for supercapacitors: experimental and first-principle studies (computational workflows). Zenodo. <https://doi.org/10.5281/zenodo.8183854>
- [49] Momma K, Izumi F (2011) VESTA 3 for three-dimensional visualization of crystal, volumetric and morphology data. *J Appl Crystallogr* 44(6):1272–1276. <https://doi.org/10.1107/S0021889811038970>
- [50] Pell WG, Conway BE (2001) Analysis of power limitations at porous supercapacitor electrodes under cyclic voltammetry modulation and dc charge. *J Power Sources* 96(1):57–67. [https://doi.org/10.1016/S0378-7753\(00\)00682-0](https://doi.org/10.1016/S0378-7753(00)00682-0)
- [51] Chowdhury A, Biswas S, Singh T, Chandra A (2022) Redox mediator induced electrochemical reactions at the electrode-electrolyte interface: making sodium-ion supercapacitors a competitive technology. *Electrochem Sci Adv* 2(1):2100030. <https://doi.org/10.1002/elsa.202100030>
- [52] Gharbi O, Tran MTT, Tribollet B, Turmine M, Vivier V (2020) Revisiting cyclic voltammetry and electrochemical impedance spectroscopy analysis for capacitance measurements. *Electrochim Acta* 343(136109):136109. <https://doi.org/10.1016/j.electacta.2020.136109>
- [53] Augustyn V, Simon P, Dunn B (2014) Pseudocapacitive oxide materials for high-rate electrochemical energy storage. *Energy Environ Sci* 7(5):1597–1614. <https://doi.org/10.1039/C3EE44164D>
- [54] Boucher C, Rubel O, Zhitomirsky I (2023) Supercapacitor performance of magnetite nanoparticles enhanced by a catecholate dispersant: experiment and theory. *Molecules* 28(4):1562. <https://doi.org/10.3390/molecules28041562>
- [55] Bliem R, McDermott E, Ferstl P, Setvin M, Gamba O, Pavelec J, Schneider MA, Schmid M, Diebold U, Blaha P, Hammer L, Parkinson GS (2014) Subsurface cation vacancy stabilization of the magnetite (001) surface. *Science* 346(6214):1215–1218. <https://doi.org/10.1126/science.1260556>
- [56] Gargallo-Caballero R, Martín-García L, Quesada A, Granaos-Miralles C, Foerster M, Aballe L, Bliem R, Parkinson GS, Blaha P, Marco JF, Figuera J (2016) Co on  $\text{Fe}_3\text{O}_4$  (001): towards precise control of surface properties. *J Chem Phys* 144(9):094704. <https://doi.org/10.1063/1.4942662>
- [57] Bader RFW (1990) Atoms in molecules: a quantum theory. Oxford University Press, New York
- [58] Rojas-Cuervo AM, Rey-González RR (2023) Electronic band gap on graphene induced by interaction with hydrogen cyanide. An DFT analysis. *Chem Phys* 565:111744. <https://doi.org/10.1016/j.chemphys.2022.111744>
- [59] Zhang Y, Song Z, Miao L, Lv Y, Gan L, Liu M (2023) All-round enhancement in Zn-ion storage enabled by solvent-guided Lewis acid-base self-assembly of heterodiatomic carbon nanotubes. *ACS Appl Mater Interfaces* 15(29):35380–35390. <https://doi.org/10.1021/acsami.3c06849>
- [60] Qin Y, Song Z, Miao L, Hu C, Chen Y, Liu P, Lv Y, Gan L, Liu M (2023) Hydrogen-bond-mediated micelle aggregating self-assembly towards carbon nanofiber networks for high-energy and long-life zinc ion capacitors. *Chem Eng J* 470:144256. <https://doi.org/10.1016/j.cej.2023.144256>
- [61] Song Z, Miao L, Lv Y, Gan L, Liu M (2023)  $\text{NH}_4^+$  charge carrier coordinated H-bonded organic small molecule for fast and superstable rechargeable zinc batteries. *Angew Chem Int Ed* 135(38):e202309446. <https://doi.org/10.1002/ange.202309446>
- [62] Moradi L, Tadayon M (2018) Green synthesis of 3,4-dihydropyrimidinones using nano  $\text{Fe}_3\text{O}_4$ @meglumine sulfonic acid as a new efficient solid acid catalyst under microwave irradiation. *J Saudi Chem Soc* 22(1):66–75. <https://doi.org/10.1016/j.jscs.2017.07.004>

- [63] Janković IA, Šponjić ZV, Čmor MI, Nedeljković JM (2009) Surface modification of colloidal TiO<sub>2</sub> nanoparticles with bidentate benzene derivatives. *J Phys Chem C* 113(29):12645–12652. <https://doi.org/10.1021/jp9013338>
- [64] Maity JP, Kar S, Lin C-M, Chen C-Y, Chang Y-F, Jean J-S, Kulp TR (2013) Identification and discrimination of bacteria using Fourier transform infrared spectroscopy. *Spectrochim Acta Part A* 116:478–484. <https://doi.org/10.1016/j.saa.2013.07.062>
- [65] Dahri R, Guizani M, Yilmaz M, Mechti L, Dahri Alsu-kaibi AK, Alimi F, ben Salem R, Moussaoui Y (2022) Experimental design analysis of murexide dye removal by carbon produced from waste biomass material. *J Chem* 2022:9735071. <https://doi.org/10.1155/2022/9735071>
- [66] Aliahmad M, Nasiri Moghaddam N (2013) Synthesis of maghemite ( $\gamma$ -Fe<sub>2</sub>O<sub>3</sub>) nanoparticles by

thermal-decomposition of magnetite (Fe<sub>3</sub>O<sub>4</sub>) nanoparticles. *Mater Sci Pol* 31(2):264–268. <https://doi.org/10.2478/s13536-012-0100-6>

**Publisher's Note** Springer Nature remains neutral with regard to jurisdictional claims in published maps and institutional affiliations.

Springer Nature or its licensor (e.g. a society or other partner) holds exclusive rights to this article under a publishing agreement with the author(s) or other rightsholder(s); author self-archiving of the accepted manuscript version of this article is solely governed by the terms of such publishing agreement and applicable law.

## **Supplementary Information**

Application of murexide as a capping agent for fabrication of magnetite anodes for supercapacitors: experimental and first-principle studies

Coulton Boucher, Dalue Tang, Igor Zhitomirsky, Oleg Rubel\*

\*Department of Materials Science and Engineering, McMaster University, 1280 Main Street West, Hamilton, L8S 4L8, Ontario, Canada.

\*Corresponding author(s). E-mail(s): rubelo@mcmaster.ca;

Contributing authors: bouchc1@mcmaster.ca; tangd8@mcmaster.ca; zhitom@mcmaster.ca;

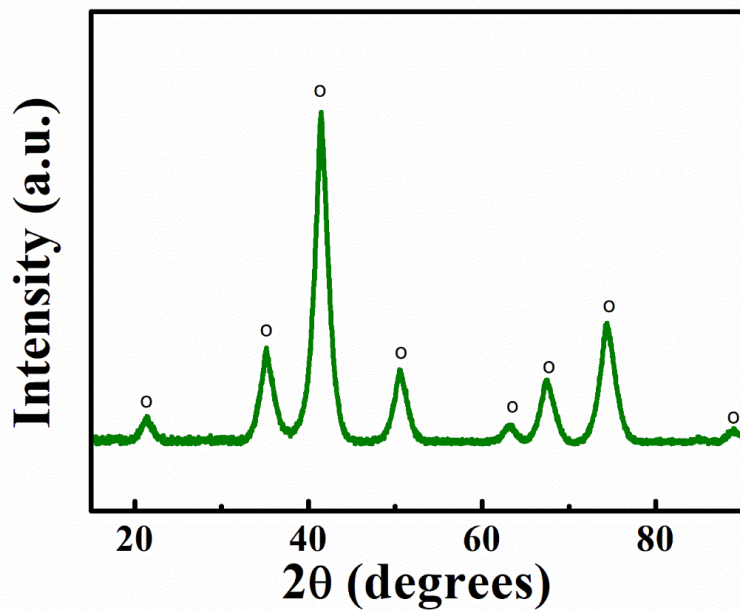


Figure S1. X-ray diffraction pattern of as-prepared  $\text{Fe}_3\text{O}_4$  (o – peaks corresponding to JCPDS file 04-007-2718). XRD testing was conducted with a diffractometer Bruker D8 Advance with Cr-K $\alpha$  radiation.

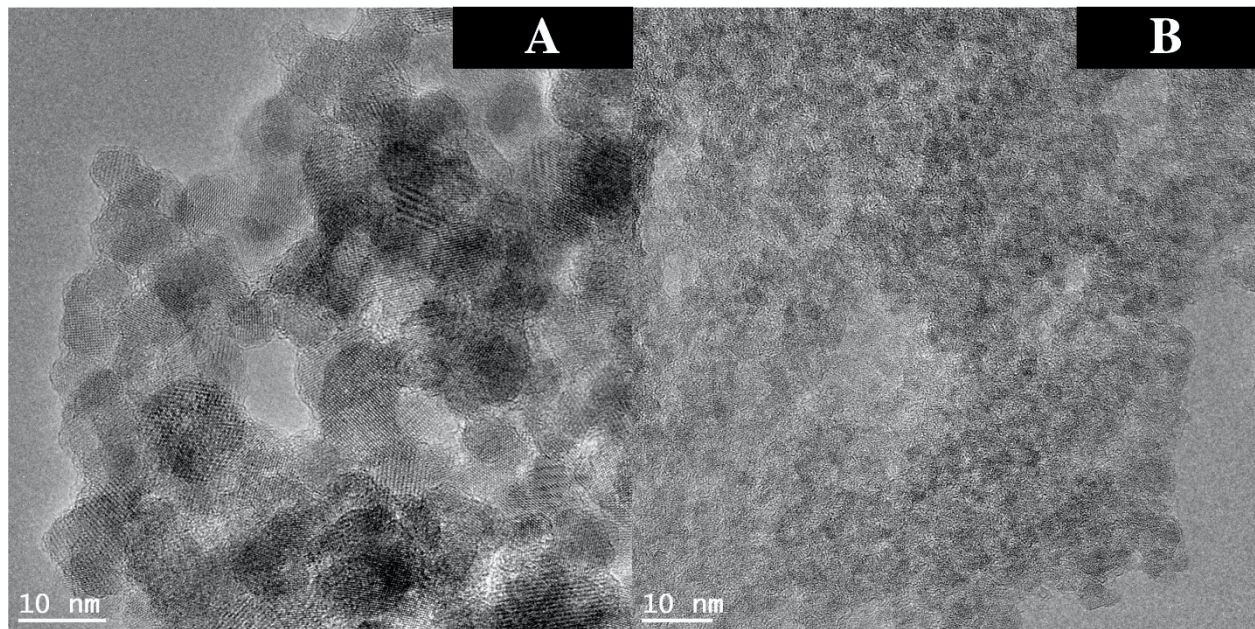


Figure S2. TEM images of  $\text{Fe}_3\text{O}_4$  particles prepared (a) without murexide and (B) with murexide as a capping agent. TALOS L102C microscope (Thermo Fisher Scientific) was used for TEM investigations.

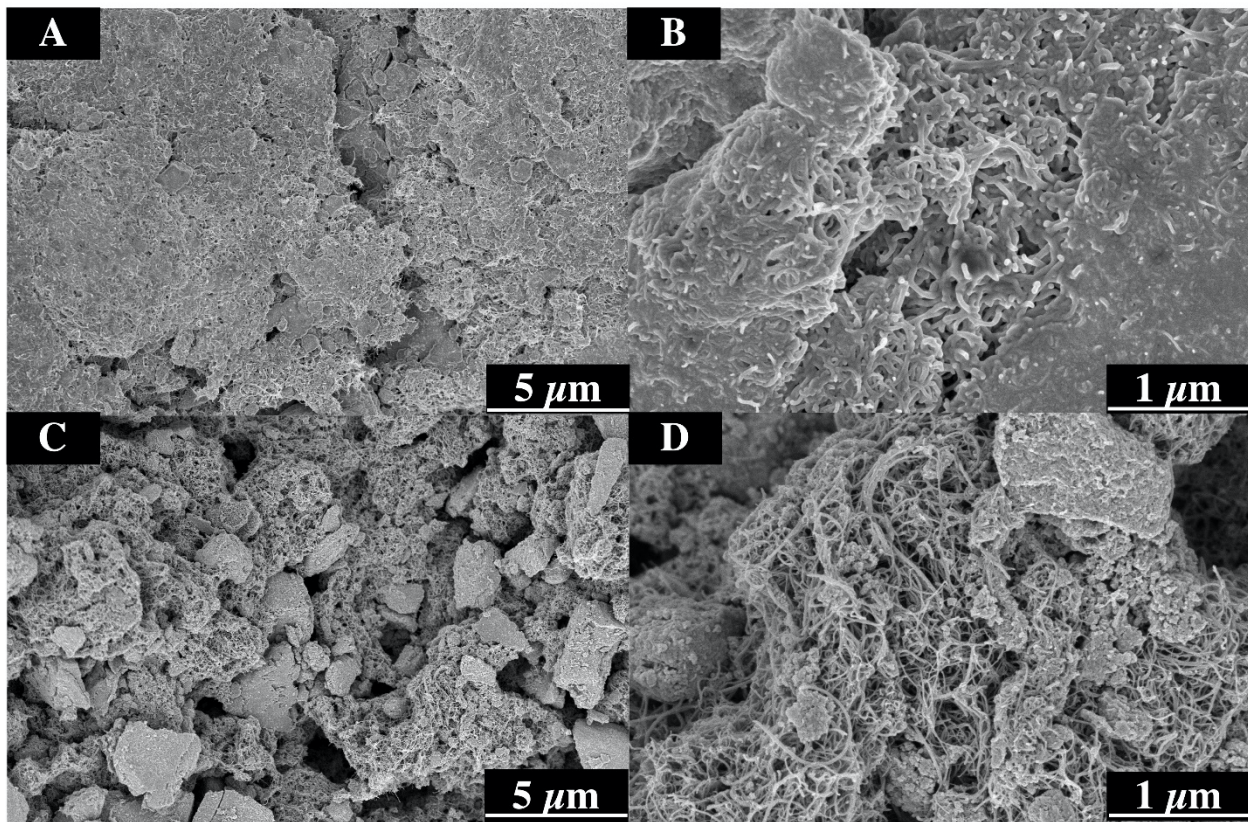


Figure S3. SEM images at different magnifications of electrodes prepared (A,B) without murexide and (C,D) with murexide as a capping agent. SEM studies were performed using FEI Magellan 400 microscope.

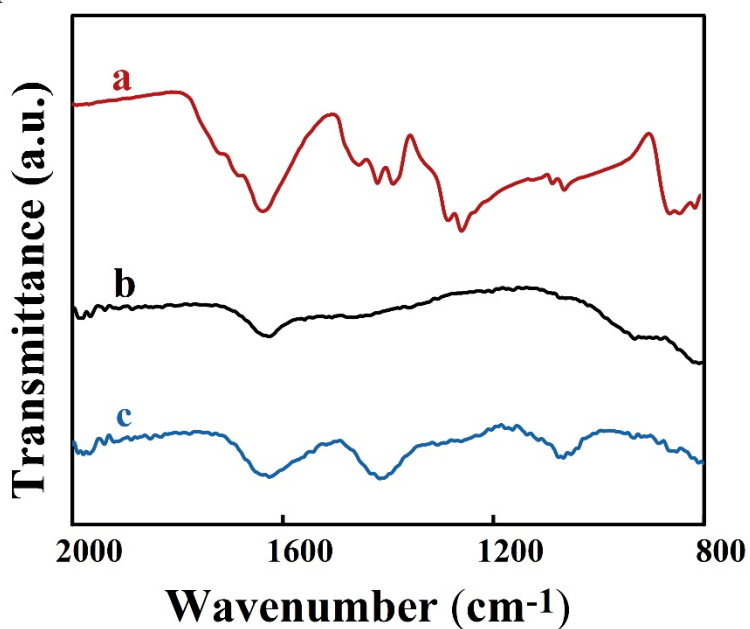


Figure S4. FTIR spectra of (a) as-received murexide, (b) as-prepared  $\text{Fe}_3\text{O}_4$  without murexide and (c) as-prepared  $\text{Fe}_3\text{O}_4$  using murexide as a capping agent. FTIR studies were conducted using a Bruker Vertex 70 spectrometer.

The broad absorption in the spectrum of murexide centered at  $\sim 1640 \text{ cm}^{-1}$  corresponds to N—H bending vibration[1]. The absorptions in the range of  $1400\text{--}1460 \text{ cm}^{-1}$  correspond to C—C and C=O stretchings, the peaks in the range of  $1260\text{--}1290 \text{ cm}^{-1}$  are related to C—N stretchings, the absorption in the range of  $1050\text{--}1090 \text{ cm}^{-1}$  is related to C—O stretching[2-5]. The broad peak in the spectrum of  $\text{Fe}_3\text{O}_4$  at  $\sim 1631 \text{ cm}^{-1}$  is related to vibrations of surface OH groups[6], which were formed during synthesis from aqueous solutions.

From the comparison of the (a-c) spectra it is seen that a broad band centered at  $1638 \text{ cm}^{-1}$  in the spectrum of  $\text{Fe}_3\text{O}_4$  prepared using murexide (Figure S4c) is related to N—H vibrations of adsorbed murexide and vibrations of surface OH groups of  $\text{Fe}_3\text{O}_4$ . The broad band at  $\sim 1420 \text{ cm}^{-1}$  in the spectrum of  $\text{Fe}_3\text{O}_4$  prepared using murexide is related to C—C and C=O stretchings (Figure S4c). Such absorption was not observed in the spectrum of  $\text{Fe}_3\text{O}_4$  prepared without murexide (Figure 4Sb). The absorption in the range of  $1050\text{--}1090 \text{ cm}^{-1}$  in Figure S4c is related to C—O stretching of murexide adsorbed on  $\text{Fe}_3\text{O}_4$  particles. Such absorptions were not observed for pure  $\text{Fe}_3\text{O}_4$  (Figure S4b). Therefore, FTIR studies confirmed murexide adsorption on  $\text{Fe}_3\text{O}_4$  particles during synthesis.

## References

- [1] L. Moradi, M. Tadayon, Green synthesis of 3, 4-dihydropyrimidinones using nano  $\text{Fe}_3\text{O}_4$ @ meglumine sulfonic acid as a new efficient solid acid catalyst under microwave irradiation, Journal of Saudi Chemical Society 22(1) (2018) 66-75.
- [2] H. Gulley-Stahl, P.A. Hogan, W.L. Schmidt, S.J. Wall, A. Buhrlage, H.A. Bullen, Surface complexation of catechol to metal oxides: an ATR-FTIR, adsorption, and dissolution study, Environmental science & technology 44(11) (2010) 4116-4121.
- [3] I.A. Jankovic, Z.V. Saponjic, M.I. Comor, J.M. Nedeljkovic, Surface modification of colloidal  $\text{TiO}_2$  nanoparticles with bidentate benzene derivatives, The Journal of Physical Chemistry C 113(29) (2009) 12645-12652.
- [4] J.P. Maity, S. Kar, C.-M. Lin, C.-Y. Chen, Y.-F. Chang, J.-S. Jean, T.R. Kulp, Identification and discrimination of bacteria using Fourier transform infrared spectroscopy, Spectrochimica Acta Part A: Molecular and Biomolecular Spectroscopy 116 (2013) 478-484.
- [5] R. Dhahri, M. Guizani, M. Yilmaz, L. Mechti, A.K. Dhahi Alsukaibi, F. Alimi, R.b. Salem, Y. Moussaoui, Experimental design analysis of murexide dye removal by carbon produced from waste biomass material, Journal of Chemistry 2022 (2022).
- [6] M. Aliahmad, N. Nasiri Moghaddam, Synthesis of maghemite ( $\gamma\text{-Fe}_2\text{O}_3$ ) nanoparticles by thermal-decomposition of magnetite ( $\text{Fe}_3\text{O}_4$ ) nanoparticles, Materials Science-Poland 31 (2013) 264-268.